THE JOURNAL OF PHYSICAL CHEMISTRY A

pubs.acs.org/JPCA Article

Spectral Narrowing Accompanies Enhanced Spatial Resolution in Saturated Coherent Anti-Stokes Raman Scattering (CARS): Comparisons of Experiment and Theory

Published as part of The Journal of Physical Chemistry virtual special issue "Time-Resolved Microscopy".

Avinash K. Singh, Kalyan Santra, Xueyu Song,* Jacob W. Petrich,* and Emily A. Smith*

Cite This: *J. Phys. Chem. A* 2020, 124, 4305−4313 Read Online

ABSTRACT: We demonstrate theoretically and confirm experimentally the mechanism by which spectral narrowing accompanies enhanced spatial resolution in a saturated coherent anti-Stokes Raman scattering (CARS) signal that is demodulated at the third harmonic ($3f$) of the pump modulation frequency (f). Under these modulation conditions, theory predicts a narrowing of the full width at half-maximum (FWHM) of the CARS spectrum by a factor of 2.0 with respect to that of the spectrum obtained by demodulation at the fundamental frequency. Theory also predicts an improvement of spatial resolution by a factor of 1.7. Experimentally, narrowing of the FWHM of the CARS spectrum of 1,4-bis((*E*)-2-methylstyryl) benzene (MSB) crystals by a factor of 2.5 is observed upon saturation. Further experimental confirmation is provided from investigating diamond particles, for which spectral narrowing was enhanced by a factor of 2.8 and spatial resolution was enhanced by a factor of 2. Details of the mechanism and execution of the saturated CARS experiment are elucidated and limits to its applicability are suggested, one of which is the conclusion that the saturation approach is not suitable for extraction of harmonics beyond $3f$. In this work, we have developed a more comprehensive understanding of the correlation between the observed experimental results and experimental factors than has been previously reported.

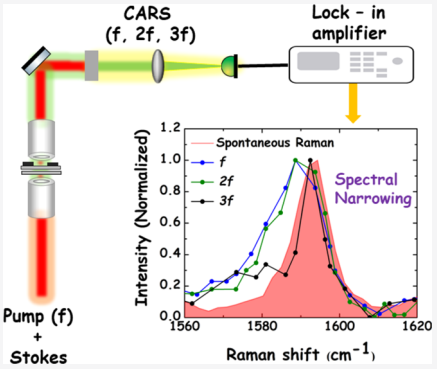

INTRODUCTION

Achieving vibrational subdiffraction imaging is an ongoing quest,[1−6] interest in which has been motivated by the successful implementation of fluorescence techniques like stimulated emission depletion (STED),[7] structured-illumination microscopy,[8] stochastic optical reconstruction microscopy (STORM),[9] and photoactivated localization microscopy (PALM).[10] These methods have made it possible to probe samples with features that are sub-10 nm on a routine basis. The fluorescence technique most relevant to our discussion exploits the saturated excitation of fluorescence (SAX), pioneered by Fujita and co-workers.[11−14] SAX provides enhanced spatial resolution by using the nonlinearity induced in the fluorescence signal at higher incident laser powers. In principle, its spatial resolution is limited only by the highest harmonic that can be measured. In practice, the limitation on spatial resolution is imposed by the shot noise of the detector, which becomes increasingly significant as the signal strength decreases with successively higher harmonics.[11] Although fluorescence techniques are successful in revealing intricate details, their application often requires the use of extrinsic organic fluorophores for labeling samples, especially in biological applications. This introduces two limitations. First, the experiment provides information on the system indirectly through the label. Second, labels can photobleach under laser irradiation and, more importantly, may be cytotoxic.[15] Vibrational imaging provides a powerful alternative because it is able to exploit the chemical functionalities already present in the sample. This presents the added benefit of eliminating additional sample preparation.

The advent of coherent Raman techniques has contributed to the popularization of label-free vibrational imaging.[16,17] Coherent anti-Stokes Raman scattering (CARS) and stimulated Raman scattering (SRS) are the two most widely used coherent Raman spectroscopies, and they have been successfully implemented in various laboratories.[18−23] In addition to providing much larger signals than those of traditional spontaneous Raman spectroscopy, the near-infrared wavelengths that are usually used for CARS and SRS penetrate deeper into tissues compared to the wavelengths used for fluorescence imaging. The penetration depth of the applied

Received: March 18, 2020
Revised: April 27, 2020
Published: May 4, 2020

https://dx.doi.org/10.1021/acs.jpca.0c02396
J. Phys. Chem. A 2020, 124, 4305−4313

wavelengths is obviously a critical parameter for imaging thick biological samples.[24]

Theoretical and experimental studies have already been performed in the area of subdiffraction coherent Raman microscopy.[5,25−29] Silva et al.[28] demonstrated the elimination of the vibrational signal from the edges of a diffraction-limited spot using a doughnut-shaped decoherence pulse. This resulted in a focal spot smaller than the diffraction limit. Bi et al. employed visible wavelengths instead of near-infrared wavelengths for SRS imaging by frequency-doubling the pump and the Stokes beam bringing the spatial resolution down to 130 nm in a near-resonance-enhanced SRS microscopy experiment.[30] As an extension of SAX, Yonemaru et al. used saturation of CARS at high power densities to induce nonlinearity in the CARS signal leading to the generation of higher harmonics of the excitation pulse modulation frequency.[5] A lock-in amplifier demodulated the higher harmonics of the signal frequency, and the image constructed by the third harmonic of the signal provided better spatial resolution than that constructed using the fundamental frequency. Enhanced spectral resolution was also observed.

Because of the high laser intensities required for these experiments that are designed to improve spatial resolution, a common feature is to test them with what are traditionally believed to be robust, highly photostable samples, *i.e.*, diamond particles.[5,28] In this work, however, to examine the suitability of the saturated CARS technique to other chemical systems and obtain a thorough and rigorous physical understanding of the experimental observations, we have studied a model organic molecule, 1,4-bis(2-methylstyryl)benzene (MSB), in addition to diamond particles. (Because MSB was interrogated as a single crystal, it could only provide information on the spectral characteristics of the technique, while the diamond samples provided both spectral and spatial information.) Our results, limited to data collected at the third harmonic ($3f$) of the modulation frequency (f), show that both the spectral and spatial resolution are improved by a factor of ∼2 with respect to that collected at the fundamental and second harmonics. Furthermore, our calculations indicate that enhancement cannot occur at the second harmonic. This is also confirmed experimentally. Finally, an important practical observation of this work is that it was necessarily limited to the third harmonic. This is because the MSB signal was too weak to observe at the fourth harmonic and because laser intensities required to observe the signal from diamond at the fourth harmonic often destroyed the sample, despite its putative robustness.

EXPERIMENTAL SECTION

Sample Preparation. 1,4-Bis(2-methylstyryl)benzene (MSB) (Figure 1) was purchased from Sigma-Aldrich and was recrystallized using toluene. A single crystal was mounted between two clean microscopy coverslips (Corning, thickness 0.16−0.19 mm) and sealed with nail varnish. Diamond particles were purchased from Tomei Diamonds (IRM 2−4, Tokyo, Japan). An ∼2 mg/mL solution of the diamond particles was drop-casted on a clean coverslip and air-dried. The diamond particles employed had an average diameter of around 2−3 μm and were identical to those used by Yonemaru et al.[5]

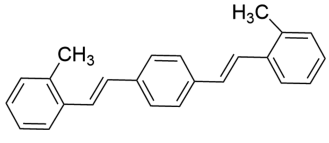

Figure 1. Structure of 1,4-bis((*E*)-2-methylstyryl) benzene.

Instrumentation. *Spontaneous Raman Spectroscopy.* Spontaneous Raman measurements were performed with an XploRA Plus Raman confocal upright microscope equipped with a Synapse EMCCD camera (HORIBA Scientific, Edison, New Jersey). The sample was excited with 16 mW of a 785 nm laser source focused on the sample with a 100×, 0.9 numerical aperture (NA) objective. Raman spectra were collected using a 1200 grooves/mm grating and with a total acquisition time of 1 s for MSB and 3 s for diamond particles. An average of two accumulations is reported.

CARS Apparatus: Modulation of the Intensity of the Pump Beam. The schematic for our CARS microscopy apparatus is presented in Figure 2 and is based on the layout

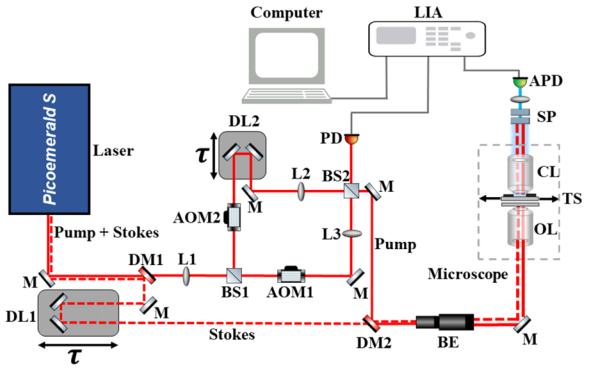

Figure 2. The CARS apparatus. Mirror (M), dichroic mirror (DM), delay line (DL), lens (L), 50:50 nonpolarizing beam splitter (BS), acousto-optical modulator (AOM), beam expander (BE), objective lens (OL), translation stage (TS), condenser lens (CL), shortpass filter (SP), photodiode (PD), avalanche photodiode (APD), and lock-in amplifier (LIA).

reported by Fujita and co-workers.[5] It is based on a one-box picosecond laser source (PicoEmerald S, APE, Berlin) with a repetition rate of 80 MHz and a pulse width of 2.3 ps. It provides a tunable pump beam (720−990 nm) and a Stokes beam fixed at 1031 nm. The pump and Stokes beams exit the laser aperture collinearly and are separated by a dichroic shortpass filter (Edmund Optics part #86-695, cutoff 1000 nm). We subsequently used a Mach−Zehnder interferometer to modulate the pump beam.[5] First, the pump beam was split using a 50:50 nonpolarizing beam splitter (Edmund Optics part #47-012). Each arm of the split pump beam was passed through an acousto-optical modulator (AOM) (AOM-402AF3, IntraAction Corp., Bellwood). One AOM was driven at 40 MHz and the other at 40.50 MHz using a dual-channel radio frequency (RF) driver (DFE-404A4, IntraAction Corp.). The first-order diffracted beams from both the AOMs were then recombined using a second beam splitter to give a beam intensity modulated at the difference frequency of the two AOMs (500 kHz). The selection of a fundamental frequency of 500 kHz was guided by our goal to detect the weak $3f$ signal above the laser noise. As the theoretical studies discussed below suggest, generating the $3f$ signal requires saturation of the CARS, and the $3f$ signal is weaker than those at f and $2f$. Accordingly, the experimental parameters had to be adjusted to

https://dx.doi.org/10.1021/acs.jpca.0c02396
J. Phys. Chem. A 2020, 124, 4305−4313

optimize the signal strength: the laser power density at the sample, the NA of the condenser lens used for the collection of the signal, the detector gain, the lock-in amplifier sensitivity, or both. The imposition of the modulation frequency on the pulse train was monitored with an oscilloscope (Agilent Infiniium 54830B DSO) (Figure S1, Supporting Information). To obtain efficient diffraction of the pulse train (and, consequently, modulation depth) and to obtain the highest beam quality, the pump beam was directed into the AOM with a 500 mm focal length lens. Identical lenses were used to collimate the first-order diffracted beams. A retroreflector mounted on a computer-controlled delay stage (Physik Instrumente, M-410.CG) was used in one of the arms of the interferometer for compensating the temporal mismatch between the two beams at recombination. After the recombination at the second beam splitter, one part of the beam was detected by a photodiode (Thorlabs DET025A) and served as the reference frequency (f) for the lock-in amplifier (model SR865A, Stanford Research Systems). A variable neutral-density filter was placed in front of the photodiode to prevent saturation of the photodiode. The second part of the beam was recombined with the Stokes beam using a dichroic, long-pass filter (Edmund Optics part #87-047, 1000 nm cutoff). A second retroreflector mounted on a computer-controlled delay stage was used in the path of the Stokes beam to ensure temporal overlap between the pump and Stokes beams in cases where the 20 ps internal delay of the laser was not enough to compensate for the path difference between the two paths. After recombination, the pump and the Stokes beams were spatially filtered and expanded (8×) with a homemade beam expander to match the back aperture of the objective lens (Nikon Plan Apo, 60×, 1.27 NA water immersion) and fed into the back port of an optical microscope (Nikon Eclipse Ti2). The CARS signal was collected in the forward mode using a 1.4 NA oil immersion condenser lens (Nikon HNA-oil) and detected by a Hamamatsu C10508-01 avalanche photodiode (APD). A stack of shortpass filters (ET850sp-2p, Chroma Technologies, 850 nm cutoff) and one bandpass filter (FF01-769/41-25, Semrock for MSB; FF01-810/10-25, Semrock for diamond particles) were used to reject the pump and the Stokes beam. The fundamental and higher harmonics of the CARS signal were detected and demodulated using the lock-in amplifier. The SR865A lock-in amplifier is capable of extracting up to the 99th harmonic of the reference frequency if $nf < 4$ MHz, where n is the nth harmonic and f is the reference frequency. CARS and saturated CARS spectra were constructed by detuning the pump wavelength in small steps (typically 0.2−0.4 nm) to cover the full range of the Raman band under consideration with a sufficient number of points and demodulating the signal at f, $2f$, and $3f$. Image construction was performed by scanning the sample over the pump and Stokes beams using an xyz-piezo stage (Nano-LP200, Mad city labs) and demodulating the signal at f and $3f$ at each pixel. Data and image acquisition were performed using GPScan.VI,[31] a Labview-based program for image scanning with a National Instruments multifunction I/O device (PCIe-6353). Fiji-ImageJ package[32] was used for image analysis.

High numerical aperture condenser lenses were used for signal collection because of their large light-gathering capability; they also have the additional advantage of reducing the background noise caused by processes such as cross-phase modulation.[17] In addition to the different power requirements for the f and the $3f$, the measurement of a reproducible signal with a good signal-to-noise ratio required adjustment of the detector parameters and the lock-in settings. Depending on the alignment and the incident power, the f and $2f$ signals were readily measured with a low detector gain (30−50) compared to the $3f$ signal, which needed adjustment of the detector gain to higher values (150). The lock-in time constant was set at 300 μs with a dwell time of 1 ms for the signal measurement at f, $2f$, and $3f$. In this work, we have limited our discussion only up to the $3f$ signal. For MSB, higher harmonics (>$3f$) could not be detected under the maximum available power density in the sample plane (12 MW/cm^2). While in the case of MSB, sample damage did not occur at these power densities, it did for the diamond particles. Thus, sample degradation of the diamond particles prevented acquisition of data at harmonics greater than $3f$.

RESULTS AND DISCUSSION

Theory. The basis of the enhancement of the spectral and spatial resolution in coherent anti-Stokes Raman scattering microscopy is the saturation of the vibrational population difference at high laser powers.[5] This intrinsically nonlinear effect[33] saturates the intensity of the CARS signal and induces additional nonlinearity in it. If, therefore, one of the lasers is modulated with a sinusoidal intensity variation, higher harmonics of that modulation frequency can be detected in the CARS signal. Here, we present a detailed theoretical account of the saturation effect on the enhancement of the spectral and spatial resolution in CARS microscopy.

The intensity of the CARS signal (I_{CARS}) generated at the focal plane (defined by $z = 0$) as a result of the interaction of two pump (p) photons and one Stokes (s) photon can be expressed as[34−36]

$$I_{CARS}(r, \omega_a, t) = k|\chi^{(3)}(r, \omega_a, t)|^2[I_{pm}(r, \omega_p, t)]^2 I_s(r, \omega_s) \quad (1)$$

where ω_a, ω_p, and ω_s are the frequencies of the anti-Stokes, pump, and Stokes beams, respectively. I_{pm} and I_s are the intensities of the pump and Stokes beams, respectively. $\chi^{(3)}$ is the third-order nonlinear susceptibility. $r \equiv (x, y)$ at $z = 0$ are the spatial coordinates at the sample plane. t is the time scale of the intensity modulation of the pump beam. (Note that while the experiment described above relies upon pulsed laser beams, the only time dependence that we explicitly consider in our treatment is that arising from the modulation of I_{pm}, which in turn modulates $\chi^{(3)}$ and I_{CARS}. Any intensity variations occurring on a much shorter time scale, such as those characterizing the profiles of the laser pulses or the oscillations of the optical fields, are integrated out over the modulation time scale t and therefore can be ignored.) $k = (2/\varepsilon_0 cn)^2$ is a proportionality constant (related to the conversion of the electric field to intensity), c is the speed of light, ε_0 is the permittivity of light in a vacuum, and n is the refractive index of the medium. The spatial intensity distributions of the two beams on the xy-plane at the focal spot ($z = 0$) are

$$I_j(x, y) = I_{j,0}\left(\frac{1}{2\pi\sigma_j^2}\right)\exp\left(-\frac{x^2 + y^2}{2\sigma_j^2}\right) \quad (2)$$

where j = pm or s for the modulated pump and Stokes beams, respectively. $I_{j,0}$ is the integrated intensity on the xy-plane at $z = 0$. We assume circular symmetry of the laser beam at the focal spot with σ_j as the beamwidth parameter. Although our

https://dx.doi.org/10.1021/acs.jpca.0c02396
J. Phys. Chem. A 2020, 124, 4305−4313

calculation is based on the focal plane, it can be generalized by incorporating the interaction length of the beams along the propagation direction (z-axis) into eq 1.[37,38] In our experiment, however, we did not vary the relative focus of the two beams in the z-direction, and the collinear CARS signal from the entire focal volume was collected. This is equivalent to integrating the signal in the focal volume, which eliminates the z-dependency in eq 2. Also, we note that the laser beam is not monochromatic and thus has a finite spectral width.[34] Since, however, we do not spectrally resolve the CARS signal but, rather, collect all of the light generated at given central wavelengths of the laser beams, the effect is equivalent to that of integrating the signal in the spectral domain of the laser. We, therefore, omit the spectral width of the laser in the model.

The third-order nonlinear susceptibility is

$$\chi^{(3)}(r, \omega_a, t) = \chi_R^{(3)}(r, \omega_a, t) + \chi_{NR}^{(3)} \tag{3}$$

where R and NR denote the resonant and nonresonant contributions.[39−42] The resonant component $\chi^{(3)}(r, \omega_a, t)$ is

$$\chi_R^{(3)}(r, \omega_a, t) = \frac{2\varepsilon_0 N c^4}{\hbar \omega_s^4}\left(\frac{d\sigma}{d\Omega}\right)\frac{\Delta(r, \omega_a, t)}{2[\omega_v - (\omega_p - \omega_s)] - i\Gamma} \tag{4}$$

where N is the number density, $\frac{d\sigma}{d\Omega}$ is the Raman cross section, Γ is the linewidth of the vibrational transition, ω_v is the frequency of the vibrational transition, and $\hbar$ is the reduced Planck constant. Δ is the normalized population difference between the two vibrational states involved in the transition (*i.e.*, if there is no saturation $\Delta = 1$; it is 0 for complete saturation). The nonresonant contribution imparts asymmetry to the CARS spectrum, which is shown in Figure S2, Supporting Information. Combining eqs 1, 3, and 4 yields

$$\begin{aligned} I_{CARS}(r, \omega_a, t) = k[&(a_1^2 + a_2^2)(\Delta(r, \omega_a, t))^2 \\ &+ 2a_1\chi_{NR}^{(3)}\Delta(r, \omega_a, t) + (\chi_{NR}^{(3)})^2] \\ &\times [I_{pm}(r, \omega_p, t)]^2 I_s(r, \omega_s) \end{aligned} \tag{5}$$

where

$$a_1 = \frac{2\varepsilon_0 N c^4}{\hbar \omega_s^4}\left(\frac{d\sigma}{d\Omega}\right)\frac{2[\omega_v - (\omega_p - \omega_s)]}{4[\omega_v - (\omega_p - \omega_s)]^2 + \Gamma^2} \tag{6}$$

and

$$a_2 = \frac{2\varepsilon_0 N c^4}{\hbar \omega_s^4}\left(\frac{d\sigma}{d\Omega}\right)\frac{\Gamma}{4[\omega_v - (\omega_p - \omega_s)]^2 + \Gamma^2} \tag{7}$$

The saturation of the population difference induces additional nonlinearity in the CARS signal *via* $\chi_R^{(3)}$. Because of stimulated Raman scattering (SRS), Δ becomes strongly dependent on the intensity of the pump and the Stokes lasers.[5,43] The temporal dependence of Δ on the modulation frequency can be described using the following kinetic equation

$$\begin{aligned} &\frac{1}{\Delta(r, \omega_a, t)}\frac{d\Delta(r, \omega_a, t)}{dt} \\ &= -2\left(\frac{4\pi c}{\hbar \omega_s^2}\right)^2\left(\frac{d\sigma}{d\Omega}\right)\frac{\Gamma}{4[\omega_v - (\omega_p - \omega_s)]^2 + \Gamma^2} \\ &\quad \times I_{pm}(r, \omega_p, t)\, I_s(r, \omega_s) \end{aligned} \tag{8}$$

Note that eq 8 only considers one of the several processes that contribute to the population difference (other factors such as CARS and the lifetime of the excited vibrational state have been ignored owing to their smaller contribution).[38,43] As described above, the intensity modulation of the pump beam is achieved *via* a Mach−Zehnder interferometer by mixing two frequency-shifted pump beams. The intensity of the modulated pump beam can be written as

$$I_{pm}(r, \omega_p, t) = \frac{I_p(r, \omega_p)}{2}(1 + \cos \omega_m t) \tag{9}$$

where $\omega_m = 2\pi f$ is the modulation frequency. The modulation of Δ in eq 8 depends on the time-dependent part of I_{pm} (*i.e.*, we neglect the exponential decay of the population due to the constant term because the population of v = 1 is reasonably assumed to be depleted on a time scale that is much faster than the time scale of modulation) and can be written as

$$\frac{1}{\Delta(r, \omega_a, t)}\frac{d\Delta(r, \omega_a, t)}{dt} = -\beta \cos \omega_m t \tag{10}$$

where

$$\begin{aligned} \beta = 2&\left(\frac{4\pi c}{\hbar \omega_s^2}\right)^2\left(\frac{d\sigma}{d\Omega}\right)\frac{\Gamma}{4[\omega_v - (\omega_p - \omega_s)]^2 + \Gamma^2} \\ &\times \frac{I_p(r, \omega_p)}{2} I_s(r, \omega_s) \end{aligned} \tag{11}$$

Solving the differential equation with the boundary condition $\Delta = 1$ at $t = 0$, we have

$$\Delta(r, \omega_a, t) = \exp\left(-\frac{\beta}{\omega_m}\sin \omega_m t\right) \tag{12}$$

The effect on the population difference due to modulation of the pump beam is given in Figure 3 for various intensities of the pump beam. Substituting eqs 9 and 12 in eq 5 yields

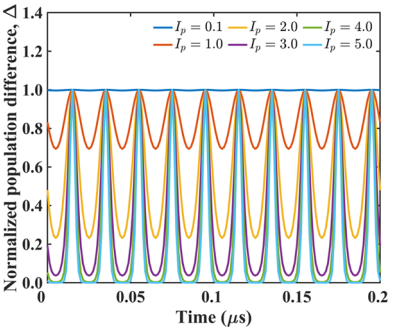

Figure 3. Effect on the population difference due to the modulation of the pump beam, at various intensities of the pump beam, for MSB. The intensity of the pump beam is given in multiples of 2.8 MW/cm^2. The intensity of the Stokes beam was fixed at 1.6 MW/cm^2. The relevant parameters for MSB are $\frac{d\sigma}{d\Omega} = 2 \times 10^{-27}$ cm^2/sr/molecule,[44] ω_v = 1593.1 cm^{-1},[44] Γ = 9.286 cm^{-1}, and $f = \frac{\omega_m}{2\pi}$ = 500 kHz. The linewidth was determined from the measurement of the spontaneous Raman spectrum and appropriate fitting of the lineshape.

https://dx.doi.org/10.1021/acs.jpca.0c02396
J. Phys. Chem. A 2020, 124, 4305−4313

$$I_{CARS}(r, \omega_a, t) = k\left[(a_1^2 + a_2^2)\exp\left(-\frac{2\beta}{\omega_m}\sin\omega_m t\right) + 2a_1\chi_{NR}^{(3)}\exp\left(-\frac{\beta}{\omega_m}\sin\omega_m t\right) + (\chi_{NR}^{(3)})^2\right] \times [I_p(r, \omega_p)]^2 I(r, \omega_s)\left(\frac{1}{2}(1 + \cos\omega_m t)\right)^2 \quad (13)$$

The CARS signal will always have DC and 2*f* components (Figure S3a,d, Supporting Information) along with a component corresponding to *f*, owing to its quadratic dependence on the pump laser intensity. However, because of the additional nonlinearity introduced by the exponential terms in I_{CARS} (eq 13), the signal will have terms corresponding to the third and even higher harmonics of *f* (Figure S3b,e, Supporting Information). The intensities of these higher-order harmonics (3*f* and greater) strongly depend on the intensity of the pump and Stokes beams and on the frequency of modulation *via* the ratio β/ω_m (*e.g.*, as shown in Figure S3c,f in comparison to Figure S3b,e of the Supporting Information). The signal in the time domain can be converted into the frequency domain to extract the frequency component of interest. Mathematically, this can be expressed as

$$I_{CARS}(r, \omega_a, F) = \mathcal{F}[I_{CARS}(r, \omega_a, t)] \quad (14)$$

where *F* denotes the modulation frequency space and $\mathcal{F}$ denotes the Fourier transform. Extraction of a signal at a multiple of the modulation frequency can be accomplished *via* a lock-in amplifier using the modulation as the reference, as described above. The signals at the fundamental and its harmonics are obtained by collecting terms in the expansion corresponding to the appropriate powers of β/ω_m. Specifically, the third harmonic will only contribute to the signal for nonzero powers of β/ω_m (as 3*f* originates solely because of the additional nonlinearity introduced by the saturation). The $\left(\frac{\beta}{\omega_m}\right)^0$ term, however, always contributes to the signal corresponding to the fundamental and second harmonic and does not necessarily require saturation of the CARS signal. (Because the signal is collected at a given harmonic, the total signal at that harmonic is normalized by dividing all terms contributing to that signal at that harmonic by the magnitude of the largest term.) The most important conclusion drawn from this analysis is that β determines both the spectral and the spatial dependence of the signal. In other words, the maximum of the harmonic component, set to 1 and demodulated at the third harmonic, will show spectral as well as spatial narrowing compared to that corresponding to the normalized fundamental and second harmonic (which are identical to each other in these respects). This will lead to resolution enhancement in both the spectral and spatial domains when the signal is collected at 3*f* or higher harmonics. Therefore, spatial resolution enhancement is fundamentally linked to the spectral resolution enhancement through the saturation of the population difference. These calculated results are presented in Figures 4 and 5 for MSB and Figures S4 and S5 of the Supporting Information for the diamond particles. Our model implies limits on the laser power. If it is sufficiently large such that higher powers of β/ω_m dominate the expansion, the terms corresponding to the third harmonic signal will diminish in relative importance with respect to those of the fundamental and second harmonic and spectral and spatial enhancement at the third harmonic will become insignificant. Under our experimental conditions, β/ω_m is ~0.002. Thus, higher-order terms can be neglected; and we should, therefore, expect spectral and spatial enhancement at the third harmonic. Our experimental data confirm our theory and calculations, as shown in Figures 6 and 7.

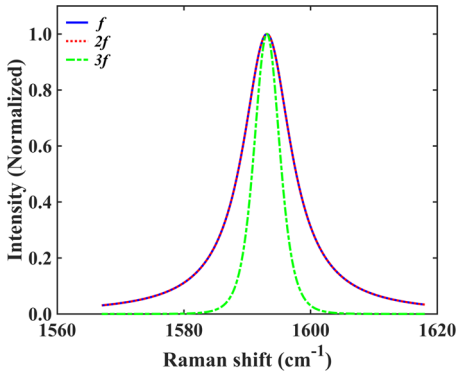

Figure 4. Saturated CARS spectra computed for MSB at *f*, 2*f*, and 3*f* show spectral narrowing only at 3*f*. The *f* and the 2*f* spectra are exactly identical. The full width at half-maximum (FWHM) for the *f* and 2*f* spectra is 9.29 cm^{-1}; that for the 3*f* spectrum is 4.70 cm^{-1}. The parameters used for the calculation of the spectra and spatial profiles of saturated CARS whose results are presented here and in Figure 5 are the same as those used for Figure 3. Owing to the absence of any values for $\chi_{NR}^{(3)}$ for MSB, we have used a value typical of organic molecules, 10^{-14} esu or 10^{-22} m^2/V^2.[45] Furthermore, for the same reason, this value has been used in our computations of the signal for diamond (Figures S4 and S5, Supporting Information).

Enhancement of Spectral Resolution in Crystals of the Organic Molecule, MSB. The Raman cross section of MSB is estimated to be 65 times that of neat benzene.[44] The 1593 cm^{-1} band of MSB was selected for the CARS experiment as it is the most intense (Figure S6, Supporting Information). The CARS spectra were constructed by demodulating the signal at the fundamental (*f*, 500 kHz), the second harmonic (2*f*, 1 MHz), and the third harmonic (3*f*, 1.5 MHz). The large MSB Raman cross section enabled the construction of the CARS spectrum by demodulating the signal at *f* and 2*f* using a pump power density of 0.8 MW/cm^2 and Stokes power density of 0.3 MW/cm^2. The robustness of our theoretical analysis is further demonstrated in that it predicts that CARS signals at both *f* and 2*f* do not require saturation (Figure S3) and that the computed spectra (Figure 4) are identical, as is demonstrated experimentally (Figure 6).

The CARS spectrum is broader than the spontaneous Raman spectrum of MSB at power densities as low as 0.8 MW/cm^2 (Figure 6). Yonemaru et al. have also reported the broadening of the CARS spectrum for the 1332 cm^{-1} band of diamond constructed by demodulating the signal at the fundamental frequency.[5] In their experiment, however, they maintained the same power levels for collecting *f* and 3*f* data and have attributed the broadening at *f* to saturation. In our case, for MSB we observed broadened CARS spectra at *f* when the pump power density was maintained either at a comparatively low excitation power density of 0.8 MW/cm^2 or at a higher excitation power density of 2.8 MW/cm^2, which was used to extract the saturated CARS signal at the third harmonic (Figure S7, Supporting Information). The broadening of the CARS spectrum at *f* can be attributed to the fast

https://dx.doi.org/10.1021/acs.jpca.0c02396
J. Phys. Chem. A 2020, 124, 4305−4313

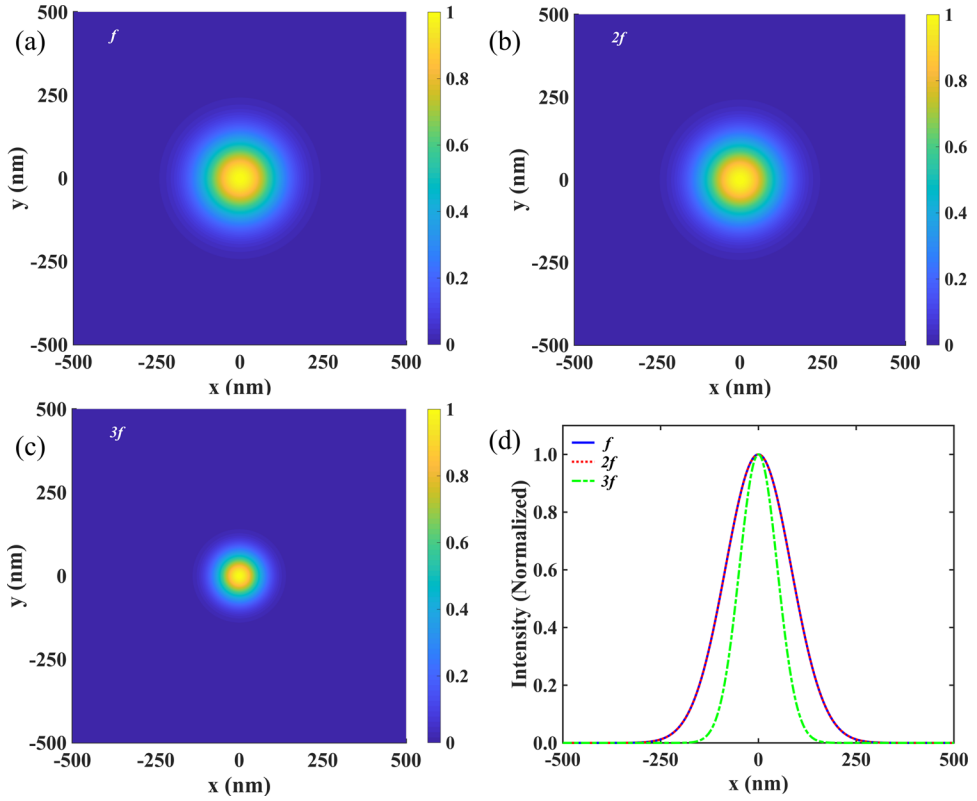

Figure 5. Calculated spatial distribution of the saturated CARS signal for MSB at f (a), $2f$ (b), and $3f$ (c), and the intensity profile (d). The FWHM determined from the intensity profile is 200 nm for both f and $2f$. It is 116 nm for $3f$. The beamwidth parameters (σ_j) for the pump beam (λ = 885.6 nm) and Stokes beam (λ = 1031 nm) were 111 and 129 nm, respectively. Other parameters used for MSB are the same as those used in calculation of the saturated CARS spectra shown in Figure 4.

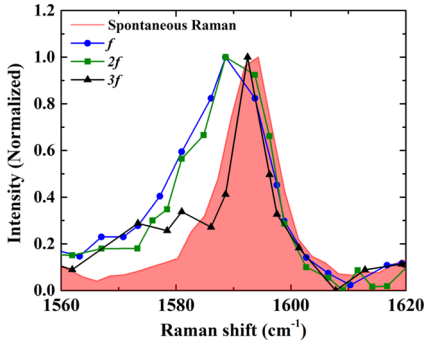

Figure 6. Comparison of experimentally obtained spectra for MSB: the spontaneous Raman spectrum (pink shaded region); CARS spectra at the fundamental (f, 500 kHz, blue), second harmonic ($2f$, 1 MHz, olive); and the saturated CARS spectrum at the third harmonic ($3f$, 1.5 MHz, black). The pump and Stokes power densities for the CARS spectra at f and $2f$ were 0.8 and 0.3 MW/cm^2, respectively, while for the saturated CARS spectrum at $3f$ the pump and Stokes power densities were 2.8 and 1.6 MW/cm^2, respectively.

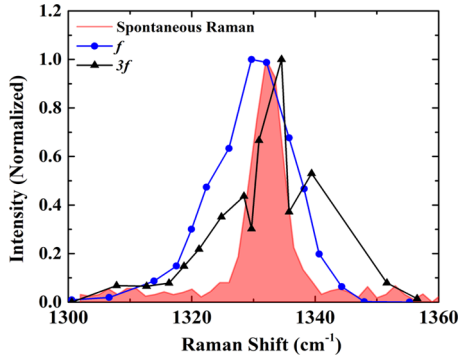

Figure 7. Spectra of diamond particles: the spontaneous Raman spectrum (shaded pink region), CARS spectrum at the fundamental (f, 500 kHz, blue), and saturated CARS spectrum at the third harmonic ($3f$, 1.5 MHz, black). The pump and Stokes power densities for the spectrum collected at f were 0.8 and 0.5 MW/cm^2, respectively; at $3f$, they were 2.2 and 1.2 MW/cm^2, respectively.

dissipation of the vibrational energy[46] in the MSB crystal as well as to the nonresonant background (NRB) contribution, which is evident from the asymmetric CARS spectrum.

For the detection of the $3f$ signal, the power densities used for the pump and the Stokes beams were 2.8 and 1.6 MW/cm^2, respectively. In another set of experiments (Figure S8, Supporting Information), we were able to reproduce the trend using 2.3 and 1.3 MW/cm^2 of pump and Stokes power density, respectively, which indicates the onset of the $3f$ signal at somewhat lower power densities compared to those used for the $3f$ data presented in Figure 6 (black curve). As shown in Figure 6, there is a significant narrowing of the $3f$ spectrum upon saturation. The FWHM of the f and $2f$ spectra is 18.3 and 17.3 cm^{-1}, respectively. In comparison, the FWHM of the $3f$ spectrum is 7.2 cm^{-1}, which corresponds to a spectral narrowing by a factor of 2.5 compared to the theoretically determined factor of 2.0. Although the asymmetry and distortion of the f and $2f$ spectra induced by the nonresonant background make it difficult to assess precisely the extent of spectral narrowing, a comparison between FWHM of the $3f$ spectrum (7.2 cm^{-1}) and the FWHM of the Lorentzian fit of

https://dx.doi.org/10.1021/acs.jpca.0c02396
J. Phys. Chem. A 2020, 124, 4305−4313

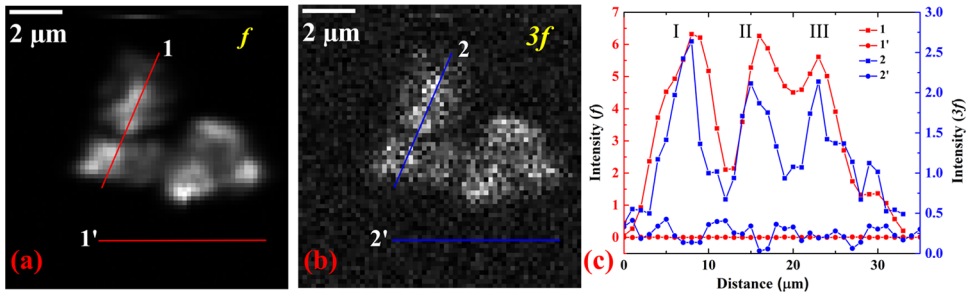

Figure 8. (a) CARS image of diamond particles collected at *f*. The pump and Stokes power densities were 0.8 and 0.5 MW/cm^2. (b) Saturated CARS image constructed by signal demodulation at 3*f*. (c) Comparison between the intensities using line profiles of two identical regions. Square markers represent intensity values for the region where diamond particles were present (1 for *f* and 2 for 3*f*) and circular markers represent intensity values for the background region (1′ for *f* and 2′ for 3*f*). Images are 64 × 64 pixels, with a lock-in time constant of 300 μs and a pixel dwell time of 1 ms.

the spontaneous Raman band (9.3 cm^{-1}) is useful (Figure 6). Also, there appears to be suppression of the nonresonant background (NRB) in the 3*f* spectrum (as opposed to the *f* and 2*f* spectra), as has been previously demonstrated for diamond.[5]

While MSB provides a useful system for exploring the applicability of saturated CARS and for testing theoretical predictions, it could only be investigated in the form of chemically homogeneous organic crystals, necessarily lacking discernible microstructures. Thus, it was not appropriate for interrogating the enhancement of spatial resolution. For this, we were obliged to resort to diamond particles.

Enhancement of Spectral and Spatial Resolution in Diamond Particles. Owing to their photostability, the high number density of tetrahedral carbon bonds, and biocompatibility, nonfluorescing diamond particles have shown promise for testing the development of new CARS imaging techniques.[5,47] Thus, we chose the 1332 cm^{-1} Raman band of diamond (Figure S9, Supporting Information) to examine the capability of our system for achieving enhanced spatial as well as spectral resolution. The diamond particles had an average size of ∼2 to 3 μm and were identical to those used by Yonemaru et al.[5] The spectra (Figure 7) and images (Figure 8a,b) corresponding to *f* and saturated 3*f* signals obtained by demodulating the signal at 500 kHz and at 1.5 MHz of the pump modulation frequency are presented. The data indicate spectral narrowing at 3*f* as compared to *f*. The FWHM of the normalized spectra at *f* (14.8 cm^{-1}) and 3*f* (5.2 cm^{-1}) reveals a narrowing by a factor of 2.8. (We note that this determination was based on the consideration of the central narrow feature of the 3*f* spectrum.) A visual comparison of the images obtained from the *f* and 3*f* data clearly shows improvements in spatial resolution (Figure 8c). As shown in Figure S4, the theoretically calculated spectral narrowing at 3*f* as compared to *f* is 2.0.

A comparison between the intensity profiles of the *f* and 3*f* images for the region where the diamond particles were present (designated as 1 and 2 Figure 8a,b) reveals three prominent features in both the *f* and 3*f* images. The 3*f* image clearly had a narrower intensity profile within a single feature. The ratio of the FWHM of the intensity profiles of feature I (Figure 8c) at *f* and 3*f* indicates an enhancement by a factor of ∼2. The theoretical calculation shows an enhancement by a factor of 1.7, as shown in Figure S5. A comparison of the background regions of *f* and 3*f* (designated as 1′ and 2′ in Figure 8a,b) indicates an inferior signal-to-noise ratio for 3*f*.

CONCLUSIONS

We have performed a theoretical analysis of the saturated CARS experiment for MSB that provides predictions concerning how the experimental parameters (notably, laser power density and modulation) affect the spectral and spatial enhancement of the signal. Computations based on the theory were compared with the experimental results obtained with an organic molecule, MSB, and diamond particles. While it is not surprising that neither spectral nor spatial enhancement should be obtained when the signal is detected at *f*, theory predicts (and experiment confirms) that the signal at 2*f* also affords no improvement in the spatial or the spectral resolution. The enhancement afforded by saturation is only attained at the third and higher harmonics of the modulation frequency. The theory correctly predicts the changes in the spectral linewidth upon saturation of the CARS, as confirmed by our experiments for MSB and diamond particles. The theory is also consistent with a previous calculation by Yonemaru et al. indicating a spatial resolution improvement of a factor of 1.27 in the lateral direction at 3*f*. We obtained a spatial resolution enhancement at 3*f* of 1.7 in our calculations and ∼2 in our experiments.

Our experimental results are limited to the third harmonic. At the fourth harmonic, the signal from MSB was too weak to be detected, and the powers required to generate a signal at the fourth harmonic often damaged the diamond particles. Thus, as has already been appreciated in the literature, there is a practical limitation to performing the saturated CARS experiment. Recently, methods like differential SAX (dSAX)[12] and virtual sinusoidal modulation (VSM)[48] have been developed to improve the signal-to-noise ratio in saturation-based techniques. dSAX, developed for saturated fluorescence microscopy, has a better efficiency in extracting a higher harmonic signal than the regular SAX experiment for the same excitation power density, thereby reducing the pixel dwell time and improving the signal-to-noise ratio.[12] Gong et al. have employed a similar strategy for high-resolution-stimulated Raman scattering imaging by VSM, which alleviates the requirement of prolonged laser exposure to accumulate sufficient signal for image generation.[48] This scheme is particularly attractive as it helps prevent photodamage of the sample.

In addition, our analysis indicates that certain ratios of the laser power to the modulation frequency, quantified by the value defined as $\frac{\beta}{\omega_m}$, can render the signal at the third harmonic negligible to those at higher harmonics. Given the high power

https://dx.doi.org/10.1021/acs.jpca.0c02396
J. Phys. Chem. A 2020, 124, 4305−4313

densities required to obtain a saturated CARS signal at the smallest possible harmonic, 3*f*, the utility of this technique is determined by maintaining a balance between the excitation power required for achieving the saturation while at the same time avoiding photodamage of the sample. In our experiments, to obtain the largest possible signals with which to test our theoretical results, we have employed strong Raman scatterers: MSB and diamond particles. But in the cases of other samples having functionalities with small Raman cross sections and low number densities for the bonds of interest, the incident power requirements may be prohibitively high. This will either require the reconsideration of experimental design or stimulate the development of algorithms for data analysis.

■ ASSOCIATED CONTENT

Supporting Information

The Supporting Information is available free of charge at https://pubs.acs.org/doi/10.1021/acs.jpca.0c02396.

Modulation waveform (Figure S1), calculated CARS spectra for MSB (Figure S2), variation of saturated CARS signal intensity with power for MSB (Figure S3), saturated CARS spectra for diamond at *f*, 2*f*, and 3*f* (Figure S4), spatial distribution of saturated CARS at *f*, 2*f*, and 3*f* for diamond (Figure S5), spontaneous Raman spectrum of MSB (Figure S6), CARS spectrum at the fundamental frequency at different powers (Figure S7), saturated CARS spectra of MSB at *f* and 3*f* (Figure S8), spontaneous Raman spectrum of diamond particles (Figure S9) (PDF)

■ AUTHOR INFORMATION

Corresponding Authors

Xueyu Song − *U.S. Department of Energy, Ames Laboratory, Ames, Iowa 50011, United States; Department of Chemistry, Iowa State University, Ames, Iowa 50011, United States;* orcid.org/0000-0001-5142-4223; Email: xsong@iastate.edu

Jacob W. Petrich − *U.S. Department of Energy, Ames Laboratory, Ames, Iowa 50011, United States; Department of Chemistry, Iowa State University, Ames, Iowa 50011, United States;* orcid.org/0000-0001-9527-6832; Email: jwp@iastate.edu

Emily A. Smith − *U.S. Department of Energy, Ames Laboratory, Ames, Iowa 50011, United States; Department of Chemistry, Iowa State University, Ames, Iowa 50011, United States;* orcid.org/0000-0001-7438-7808; Email: esmith1@iastate.edu

Authors

Avinash K. Singh − *U.S. Department of Energy, Ames Laboratory, Ames, Iowa 50011, United States*

Kalyan Santra − *U.S. Department of Energy, Ames Laboratory, Ames, Iowa 50011, United States;* orcid.org/0000-0002-2556-1889

Complete contact information is available at: https://pubs.acs.org/10.1021/acs.jpca.0c02396

Notes

The authors declare no competing financial interest.

■ ACKNOWLEDGMENTS

This research was supported by the U.S. Department of Energy, Office of Science, Office of Biological and Environmental Research (BER) through the Ames Laboratory. The Ames Laboratory is operated for the U.S. Department of Energy by Iowa State University under Contract No. DE-AC02-07CH11358.

■ REFERENCES

(1) Prince, R. C.; Potma, E. O. Going visible: high-resolution coherent Raman imaging of cells and tissues. *Light: Sci. Appl.* **2019**, *8*, No. 10.

(2) Graefe, C. T.; Punihaole, D.; Harris, C. M.; Lynch, M. J.; Leighton, R.; Frontiera, R. R. Far-field super-resolution vibrational spectroscopy. *Anal. Chem.* **2019**, *91*, 8723−8731.

(3) Upputuri, P. K.; Wu, Z.; Gong, L.; Ong, C. K.; Wang, H. Super-resolution coherent anti-Stokes Raman scattering microscopy with photonic nanojets. *Opt. Express* **2014**, *22*, 12890−12899.

(4) Gasecka, A.; Daradich, A.; Dehez, H.; Piché, M.; Côté, D. Resolution and contrast enhancement in coherent anti-Stokes Raman-scattering microscopy. *Opt. Lett.* **2013**, *38*, 4510−4513.

(5) Yonemaru, Y.; Palonpon, A. F.; Kawano, S.; Smith, N. I.; Kawata, S.; Fujita, K. Super-spatial- and -spectral-resolution in vibrational imaging via saturated coherent anti-Stokes Raman scattering. *Phys. Rev. Appl.* **2015**, *4*, No. 014010.

(6) Würthwein, T.; Irwin, N.; Fallnich, C. Saturated Raman scattering for sub-diffraction-limited imaging. *J. Chem. Phys.* **2019**, *151*, No. 194201.

(7) Hell, S. W.; Wichmann, J. Breaking the diffraction resolution limit by stimulated emission: stimulated-emission-depletion fluorescence microscopy. *Opt. Lett.* **1994**, *19*, 780−782.

(8) Gustafsson, M. G. L. Nonlinear structured-illumination microscopy: Wide-field fluorescence imaging with theoretically unlimited resolution. *Proc. Natl. Acad. Sci. U.S.A.* **2005**, *102*, 13081−13086.

(9) Rust, M. J.; Bates, M.; Zhuang, X. Sub-diffraction-limit imaging by stochastic optical reconstruction microscopy (STORM). *Nat. Methods* **2006**, *3*, 793−796.

(10) Betzig, E.; Patterson, G. H.; Sougrat, R.; Lindwasser, O. W.; Olenych, S.; Bonifacino, J. S.; Davidson, M. W.; Lippincott-Schwartz, J.; Hess, H. F. Imaging intracellular fluorescent proteins at nanometer resolution. *Science* **2006**, *313*, 1642−1645.

(11) Fujita, K.; Kobayashi, M.; Kawano, S.; Yamanaka, M.; Kawata, S. High-resolution confocal microscopy by saturated excitation of fluorescence. *Phys. Rev. Lett.* **2007**, *99*, No. 228105.

(12) Nawa, Y.; Yonemaru, Y.; Kasai, A.; Oketani, R.; Hashimoto, H.; Smith, N. I.; Fujita, K. Saturated excitation microscopy using differential excitation for efficient detection of nonlinear fluorescence signals. *APL Photonics* **2018**, *3*, No. 080805.

(13) Yamanaka, M.; Tzeng, Y.-K.; Kawano, S.; Smith, N. I.; Kawata, S.; Chang, H.-C.; Fujita, K. SAX microscopy with fluorescent nanodiamond probes for high-resolution fluorescence imaging. *Biomed. Opt. Express* **2011**, *2*, 1946−1954.

(14) Yonemaru, Y.; Yamanaka, M.; Smith, N. I.; Kawata, S.; Fujita, K. Saturated excitation microscopy with optimized excitation modulation. *ChemPhysChem* **2014**, *15*, 743−749.

(15) Ettinger, A.; Wittmann, T. Fluorescence Live Cell Imaging. In *Methods in Cell Biology*; Waters, J. C.; Wittman, T., Eds.; Academic Press, 2014; Vol. *123*, pp 77−94.

(16) Zumbusch, A.; Holtom, G. R.; Xie, X. S. Three-dimensional vibrational imaging by coherent anti-Stokes Raman scattering. *Phys. Rev. Lett.* **1999**, *82*, 4142−4145.

(17) Freudiger, C. W.; Min, W.; Saar, B. G.; Lu, S.; Holtom, G. R.; He, C.; Tsai, J. C.; Kang, J. X.; Xie, X. S. Label-free biomedical imaging with high sensitivity by stimulated Raman scattering microscopy. *Science* **2008**, *322*, 1857−1861.

(18) Evans, C. L.; Xie, X. S. Coherent anti-Stokes Raman scattering microscopy: chemical imaging for biology and medicine. *Annu. Rev. Anal. Chem.* **2008**, *1*, 883−909.
(19) Day, J. P. R.; Domke, K. F.; Rago, G.; Kano, H.; Hamaguchi, H.-o.; Vartiainen, E. M.; Bonn, M. Quantitative coherent anti-Stokes Raman scattering (CARS) microscopy. *J. Phys. Chem. B* **2011**, *115*, 7713−7725.
(20) Tipping, W. J.; Lee, M.; Serrels, A.; Brunton, V. G.; Hulme, A. N. Stimulated Raman scattering microscopy: an emerging tool for drug discovery. *Chem. Soc. Rev.* **2016**, *45*, 2075−2089.
(21) Polli, D.; Kumar, V.; Valensise, C. M.; Marangoni, M.; Cerullo, G. Broadband coherent Raman scattering microscopy. *Laser Photonics Rev.* **2018**, *12*, No. 1800020.
(22) Syed, A.; Smith, E. A. Raman imaging in cell membranes, lipid-rich organelles and lipid bilayers. *Annu. Rev. Anal. Chem.* **2017**, *10*, 271−291.
(23) Rodriguez, L. G.; Lockett, S. J.; Holtom, G. R. Coherent anti-stokes Raman scattering microscopy: A biological review. *Cytom. A* **2006**, *69A*, 779−791.
(24) Sordillo, L. A.; Pu, Y.; Pratavieira, S.; Budansky, Y.; Alfano, R. R. Deep optical imaging of tissue using the second and third near-infrared spectral windows. *J. Biomed. Opt.* **2014**, *19*, No. 056004.
(25) Beeker, W. P.; Groß, P.; Lee, C. J.; Cleff, C.; Offerhaus, H. L.; Fallnich, C.; Herek, J. L.; Boller, K.-J. A route to sub-diffraction-limited CARS Microscopy. *Opt. Express* **2009**, *17*, 22632−22638.
(26) Cleff, C.; Groß, P.; Fallnich, C.; Offerhaus, H. L.; Herek, J. L.; Kruse, K.; Beeker, W. P.; Lee, C. J.; Boller, K.-J. Stimulated-emission pumping enabling sub-diffraction-limited spatial resolution in coherent anti-Stokes Raman scattering microscopy. *Phys. Rev. A* **2013**, *87*, No. 033830.
(27) Beeker, W. P.; Lee, C. J.; Boller, K.-J.; Groß, P.; Cleff, C.; Fallnich, C.; Offerhaus, H. L.; Herek, J. L. Spatially dependent Rabi oscillations: An approach to sub-diffraction-limited coherent anti-Stokes Raman-scattering microscopy. *Phys. Rev. A* **2010**, *81*, No. 012507.
(28) Silva, W. R.; Graefe, C. T.; Frontiera, R. R. Toward label-free super-resolution microscopy. *ACS Photonics* **2016**, *3*, 79−86.
(29) Kim, H.; Bryant, G. W.; Stranick, S. J. Superresolution four-wave mixing microscopy. *Opt. Express* **2012**, *20*, 6042−6051.
(30) Bi, Y.; Yang, C.; Chen, Y.; Yan, S.; Yang, G.; Wu, Y.; Zhang, G.; Wang, P. Near-resonance enhanced label-free stimulated Raman scattering microscopy with spatial resolution near 130 nm. *Light: Sci. Appl.* **2018**, *7*, 81.
(31) Ferrand, P. GPScan.VI: A general-purpose LabVIEW program for scanning imaging or any application requiring synchronous analog voltage generation and data acquisition. *Comput. Phys. Commun.* **2015**, *192*, 342−347.
(32) Schindelin, J.; Arganda-Carreras, I.; Frise, E.; Kaynig, V.; Longair, M.; Pietzsch, T.; Preibisch, S.; Rueden, C.; Saalfeld, S.; Schmid, B.; et al. Fiji: an open-source platform for biological-image analysis. *Nat. Methods* **2012**, *9*, 676−682.
(33) Seigman, A. E. *Lasers*; University Science Books: Mill Valley, California, 1986; p 206.
(34) Marrocco, M. Spectral synthesis of coherent anti-Stokes Raman spectra with broadband Stokes lasers of arbitrary line shapes. *J. Raman Spectrosc.* **2007**, *38*, 1064−1072.
(35) Zheltikov, A. M. Coherent anti-Stokes Raman scattering: from proof-of-the-principle experiments to femtosecond CARS and higher order wave-mixing generalizations. *J. Raman Spectrosc.* **2000**, *31*, 653−667.
(36) Yueh, F. Y.; Beiting, E. J. Analytical expressions for coherent anti-stokes raman spectral (CARS) profiles. *Comput. Phys. Commun.* **1986**, *42*, 65−71.
(37) Tolles, W. M.; Nibler, J. W.; McDonald, J. R.; Harvey, A. B. A review of the theory and application of coherent anti-Stokes Raman spectroscopy (CARS). *Appl. Spectrosc.* **1977**, *31*, 253−271.
(38) Druet, S. A. J.; Taran, J.-P. E. Cars spectroscopy. *Prog. Quantum Electron.* **1981**, *7*, 1−72.
(39) Moya, F.; Regnier, R. P.; Taran, J. P. E. Gas concentration measurement by coherent Raman anti-Stokes scattering. *AIAA J.* **1974**, *12*, 826−831.
(40) Levenson, M. D.; Bloembergen, N. Dispersion of the nonlinear optical susceptibility tensor in centrosymmetric media. *Phys. Rev. B* **1974**, *10*, 4447−4463.
(41) Shen, Y. R.; Bloembergen, N. Theory of stimulated Brillouin and Raman scattering. *Phys. Rev.* **1965**, *137*, A1787−A1805.
(42) Penzkofer, A.; Laubereau, A.; Kaiser, W. High intensity Raman interactions. *Prog. Quantum Electron.* **1979**, *6*, 55−140.
(43) Magnotti, G.; Cutler, A. D.; Herring, G. C.; Tedder, S. A.; Danehy, P. M. Saturation and Stark broadening effects in dual-pump CARS of N2, O2, and H2. *J. Raman Spectrosc.* **2012**, *43*, 611−620.
(44) McCreery, R. L. *Raman Spectroscopy for Chemical Analysis*; John Wiley & Sons, Inc.: New York, Vol. *157*.
(45) Lynch, R. T., Jr.; Lotem, H. Two-photon absorption measurements in organic liquids via nonlinear light mixing spectroscopy. *J. Chem. Phys.* **1977**, *66*, 1905−1913.
(46) Fast, A.; Potma Eric, O. Coherent Raman scattering with plasmonic antennas. *Nanophotonics* **2019**, *8*, 991−1021.
(47) Pope, I.; Payne, L.; Zoriniants, G.; Thomas, E.; Williams, O.; Watson, P.; Langbein, W.; Borri, P. Coherent anti-Stokes Raman scattering microscopy of single nanodiamonds. *Nat. Nanotechnol.* **2014**, *9*, 940.
(48) Gong, L.; Zheng, W.; Ma, Y.; Huang, Z. Saturated stimulated-Raman-scattering microscopy for far-field superresolution vibrational imaging. *Phys. Rev. Appl.* **2019**, *11*, No. 034041.

https://dx.doi.org/10.1021/acs.jpca.0c02396
J. Phys. Chem. A 2020, 124, 4305−4313